

The Advantage of Nanowire Configuration in Band Structure Determination

Mirjana Dimitrievska,* Fredrik S. Hage, Simon Escobar Steinvall, Alexander P. Litvinchuk, Elias Z. Stutz, Quentin M. Ramasse, and Anna Fontcuberta i Morral*

Earth-abundant and environmentally friendly semiconductors offer a promising path toward low-cost mass production of solar cells. A critical aspect in exploring new semiconducting materials and demonstrating their enhanced functionality consists in disentangling them from the artifacts of defects. Nanowires are diameter-tailored filamentary structures that tend to be defect-free and thus ideal model systems for a given material. Here, an additional advantage is demonstrated, which is the determination of the band structure, by performing high energy and spatial resolution electron energy-loss spectroscopy in a loof and inner beam geometry in a scanning transmission electron microscope. The experimental results are complemented by spectroscopic ellipsometry and are excellently correlated with first principles calculations. This study opens the path for characterizing the band structure of new compounds in a non-destructive and prompt manner, strengthening the route of new materials discovery.

synthesize the compound and to demonstrate the functionality. A particular criterion in selecting the most suitable, stable, and functional materials to synthesize is the abundance of the elements employed. Large area applications like solar cells can only be deployed broadly if the fabrication is sustainable in the long term.

A key issue in characterizing newly synthesized materials is the distinction between the fabrication defects and their intrinsic properties. The creation of novel materials takes time to optimize. The sooner one can disentangle the role of defects from the predicted functionality, the faster the material can be adopted/embraced/retained.


Nanowires are filamentary single-crystal structures. Among many intrinsic advantages, they can be fabricated in a single-crystal form without stacking faults or antiphase boundaries.^[17–21] Synthesizing a new material in nanowire form provides a path to precisely characterize its functionality. Now, given the reduced size of nanowires, challenges arise as most characterization techniques are adapted to thin film or bulk materials. Here, we demonstrate the potential of electron microscopy to unveil not only the structure down to the atomic scale, but also the optical

1. Introduction

Machine learning and advanced simulation and modeling techniques have driven the fast screening and discovery of materials.^[1–7] Among many endeavors, this effort has helped identify valid candidates for energy conversion applications.^[7–16] After the materials' existence and/or properties are predicted in silico, the task is turned to experimental material scientists to

Dr. M. Dimitrievska, Dr. S. Escobar Steinvall, E. Z. Stutz, Prof. A. Fontcuberta i Morral
Laboratory of Semiconductor Materials
Institute of Materials
Faculty of Engineering
Swiss Federal Institute of Technology (EPFL)
Lausanne 1015, Switzerland
E-mail: mirjana.dimitrievska@epfl.ch; anna.fontcuberta-morral@epfl.ch
Prof. F. S. Hage, Prof. Q. M. Ramasse
SuperSTEM Laboratory
SciTech Daresbury Campus
Keckwick Lane, Warrington WA4AD, UK

Prof. F. S. Hage
Department of Materials
University of Oxford
Oxford OX1 3PH, UK
Prof. F. S. Hage
Department of Physics/Centre for Materials Science
and Nanotechnology
University of Oslo
Oslo NO-0318, Norway
Prof. A. P. Litvinchuk
Texas Center for Superconductivity and Department of Physics
University of Houston
Houston, TX 77204-5002, USA
Prof. Q. M. Ramasse
School of Chemical and Process Engineering and School of Physics
and Astronomy
University of Leeds
Leeds LS2 9JT, UK
Prof. A. Fontcuberta i Morral
Institute of Physics
Faculty of Basic Sciences
Swiss Federal Institute of Technology (EPFL)
Lausanne 1015, Switzerland

 The ORCID identification number(s) for the author(s) of this article can be found under <https://doi.org/10.1002/adfm.202105426>.

© 2021 The Authors. Advanced Functional Materials published by Wiley-VCH GmbH. This is an open access article under the terms of the Creative Commons Attribution License, which permits use, distribution and reproduction in any medium, provided the original work is properly cited.

DOI: 10.1002/adfm.202105426

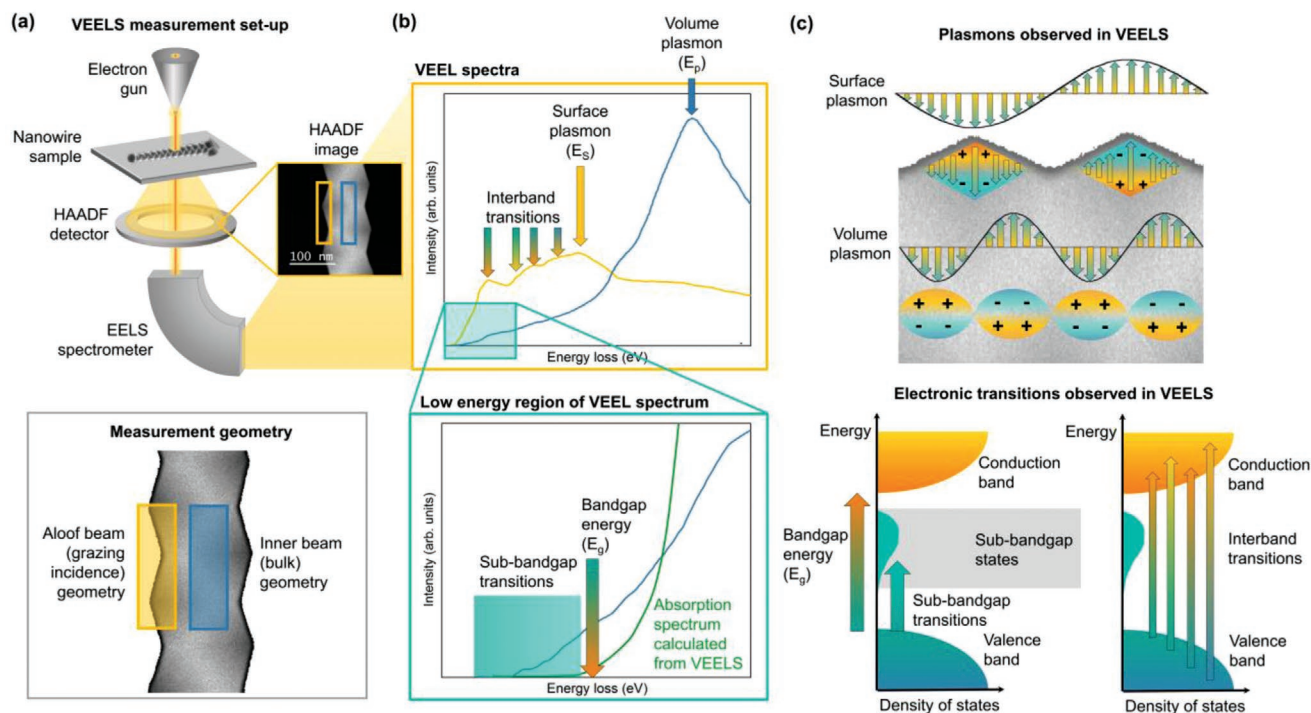


Figure 1. Electronic band structure determination in semiconductors using VEELS: a) Schematic illustration of VEEL spectrum acquisition in STEM (top panel), along with representation of two measurements geometries, bulk and aloof beam (bottom panel), which allows a clear distinction between surface and bulk contributions of the energy loss function. Aloof beam geometry, where measurements are done at the edge of the material, allows for investigating surface losses, without a strong contribution from the volume plasmon. In contrast, VEEL spectra measured in inner beam geometry, where the beam is completely positioned on the material, are usually dominated by the volume plasmon. b) Example of VEEL spectra measured in both geometries (top panel), and magnified low energy region (bottom panel). Different energy regions correspond to various optoelectronic processes occurring in materials, and can be attributed to bandgap energy, subbandgap and interband transitions, and coherent electron oscillations (surface and volume plasmons). c) Graphical illustration of different physical phenomena observed in the VEEL spectra, allowing a complete experimental fingerprint of the electronic band structure in various semiconductor materials.

functionality. This work provides a concrete path toward the utilization of electron energy loss spectroscopy for the fast throughput characterization of the optical performance of novel materials. As a model material system, we chose zinc phosphide (Zn_3P_2) nanowires, a compound semiconductor made of earth-abundant elements extremely promising for solar energy harvesting applications.

A transmission electron microscope allows for much more than the characterization of the material's structure. Electron-matter interactions provide means of understanding the composition and the band structure by the excitation of electronic states.^[22–24] Collecting the electron excited-photons at the X-ray or around the visible/UV domain provides direct information on the material composition and light emitting properties down to the atomic scale.^[25] Capturing the energy loss spectra of electrons is also often used to map elemental composition. Interestingly, the energy-loss function contains information on the band structure. The so-called valence electron energy loss spectroscopy (VEELS) technique reports on the excitations of valence electrons, such as collective plasma oscillations and single-electron transitions that depend upon the position of electronic levels within the band structure.^[26] Recent instrumental developments involving the monochromaticity of the beam and the spectral resolution in the energy loss have advanced this technique. These clearly provide new avenues for the characterization of materials.^[27,28]

Figure 1a portrays the experimental setting of this work. VEELS measurements were performed in a scanning transmission electron microscope (STEM). Relativistic electrons with de Broglie wavelengths at the picometer level and energies of 60 keV are focused and monochromated through a series of electromagnetic lenses to form a sub-Ångström sized electron probe. This electron beam scans the sample with atomic resolution, in our case a Zn_3P_2 nanowire. The incident electron beam can interact inelastically with the sample, which in the lower-loss region may result in either interband excitations (e.g., valence to conduction band transitions) or collective electron excitations, also known as plasmons, which are observed in energy-loss spectra. The energy spectrum of the electrons with 30 meV resolution (as estimated by the full-width at half-maximum of the zero-loss peak [ZLP] in vacuum: see Experimental Section for details) was collected after passing through the nanowire (Figure 1b). Plasmons can be excited either in the bulk or edge of the material as depicted in Figure 1c. Detailed information on the structure is acquired with a high-angle annular dark-field (HAADF) detector, which collects electrons that are scattered at high angles.

VEELS experiments are performed in two distinct configurations by exciting the center, or edge of the nanowires. We refer to these, respectively, as bulk and aloof beam geometries (Figure 1b). Electron energy losses detected at the bulk of the sample are strongly dominated by the so-called bulk plasmon, and also reflect

electron excitations of core electrons. The aloof beam or grazing incidence geometry corresponds to measurements performed at the edge of the material. Given the non-squared cross section of the nanowires, the material thins toward the edge, giving access to losses due to surface related plasmon excitations, without a strong contribution from the volume plasmon. One should note that bulk or inner beam geometry measurements, which are performed directly on the material, result in the EEL spectrum being a linear combination of both the bulk and surface energy loss functions. As depicted in Figure 1c, plasmons originate from coherent electron oscillations triggered by their response to the repulsive field carried by the incident electron. This provides a fingerprint of the electronic structure of the material. The combination of both grazing and bulk measurement geometries provides complementary information on electronic transitions as well as detailed characterization of surface and volume plasmons. The nanowire geometry intrinsically provides these two measurement configurations without the risk of having defected surfaces, as is typical of electron microscopy lamellae. Nanowire structures also release the strain resulting from heterostructures, freeing up an additional potential artifact.

2. Results and Discussion

We move now to demonstrate the use of VEELS on Zn₃P₂ nanowires for a complete determination of the electronic band structure. Zn₃P₂ is a tetragonally structured semiconductor (space group *P4₂/nmc* (*D_{4h}¹⁵*)) with a direct bandgap at 1.5 eV, high absorption coefficient of 10⁴–10⁵ cm⁻¹, and carrier diffusion lengths of ≈10 μm.^[29–35] Current record solar cells have efficiencies of up to 6%,^[36] which is well below their theoretical limit (>30%),^[37] illustrating the improvement potential of this material.^[37] While recent breakthrough in synthesis of highly crystalline Zn₃P₂ using innovative nanoscale methods (e.g., selective area epitaxy)^[35,38,39] have rekindled the interest in the material, major limitations related to controllable optoelectronic properties^[31,32,34,40–47] and device design still need to be resolved. This is the reason why precise determination of the electronic properties of Zn₃P₂ is of uttermost importance.

2.1. Dielectric Function of Zinc Phosphide

Representative secondary electron SEM images of a typical zigzag Zn₃P₂ nanowires used in this study are shown in Figure 2a,b. These nanowires grow through the stacking of (101) planes, with side facets also belonging to {101}. Compositional assessment, performed by energy dispersive X-ray spectroscopy coupled with STEM, has shown a homogenous distribution of Zn and P with no phase segregation (Figure S1, Supporting Information). Additional structural and compositional characterization of these nanowires is presented in ref. [38]. Figure 2c shows the HAADF-STEM image of the regions on which VEELS measurements have been performed in both bulk and aloof beam geometries.

Figure 2d presents the VEEL spectra of the Zn₃P₂ nanowire measured in inner and aloof beam geometry after the ZLP and multiple scattering have been subtracted. It should be noted that

Cherenkov losses which become dominant only in thicker samples (typically thicknesses greater than 0.6 times the mean free path length)^[48,49] or for very small collection angles (few μrad),^[50] have been neglected in these cases. This is consistent with the homogeneity of the VEEL spectra obtained on nanowire regions with different thicknesses (Figure S2, Supporting Information) as a relatively low acceleration voltage (60 kV) was used.

VEEL spectra are directly related to the energy loss function, which is defined as the imaginary part of the negative inverse dielectric function $\text{Im}[-1/\epsilon(q, E)]$, where $\epsilon(q, E) = \epsilon_1 + i\epsilon_2$ is the complex dielectric function of the material at energy loss E and the momentum transfer q . In order to extract the dielectric function, it is first necessary to perform a decomposition into bulk and surface contributions of the experimental VEEL spectrum measured in inner beam geometry. The underlying assumption is that the single scattering cross section can be expressed as a linear combination of the bulk $\text{Im}[-1/\epsilon(\omega)]$ and surface $\text{Im}[-1/(1 + \epsilon(\omega))]$ energy loss functions:^[51,52]

$$\text{Im}\left[-\frac{1}{\epsilon}\right] = \frac{\epsilon_2}{\epsilon_1^2 + \epsilon_2^2} \quad (1)$$

$$\text{Im}\left[-\frac{1}{\epsilon + 1}\right] = \frac{\epsilon_2}{(\epsilon_1 + 1)^2 + \epsilon_2^2} \quad (2)$$

where ϵ_1 and ϵ_2 are the real and imaginary parts of the total dielectric function ϵ . Here, we note that Equations (1) and (2) are typical for bulk materials, and can be modified in case of nanomaterials due to quantum confinement effects, as explained in ref. [26]. However, considering that the size of Zn₃P₂ nanowire used in this study (Figure 2c) is significantly higher than the Bohr radii for Zn₃P₂ (around 10 nm^[53,54]), no quantum confinement effects are expected,^[55] and the whole system can be treated from bulk material perspective.

The dielectric functions were extracted using Kramers–Kronig analysis.^[27] This includes numerically calculating the function $\text{Re}[1/\epsilon(\omega)]$ from $\text{Im}[-1/\epsilon(\omega)]$ by using the following relation:

$$\text{Re}\left[-\frac{1}{\epsilon}\right] = 1 - \frac{2}{\pi} P \int_0^\infty \text{Im}\left[-\frac{1}{\epsilon(\omega')}\right] \frac{\omega' d\omega'}{\omega'^2 - \omega^2} \quad (3)$$

where P denotes the Cauchy principal part of the integral, avoiding the pole at $\omega = \omega'$. It should be noted that the factor $\omega'/(\omega'^2 - \omega^2)$ acts as a “weighting function,” giving prominence to energy losses $\hbar\omega'$, which are close to $\hbar\omega$.

Complementary measurements of the refractive index of Zn₃P₂ were performed by spectroscopic ellipsometry. In this case, the real (ϵ_1) and imaginary (ϵ_2) part of the dielectric function were derived according to the following relations:

$$\epsilon_1(E) = n^2 - k^2 \quad (4)$$

$$\epsilon_2(E) = 2nk \quad (5)$$

where n and k are the refractive index and extinction coefficients, respectively. As a reference, we used monocrystalline Zn₃P₂ thin films.^[56] Figure 2e shows the resulting values of the refractive index obtained by spectroscopic ellipsometry. The

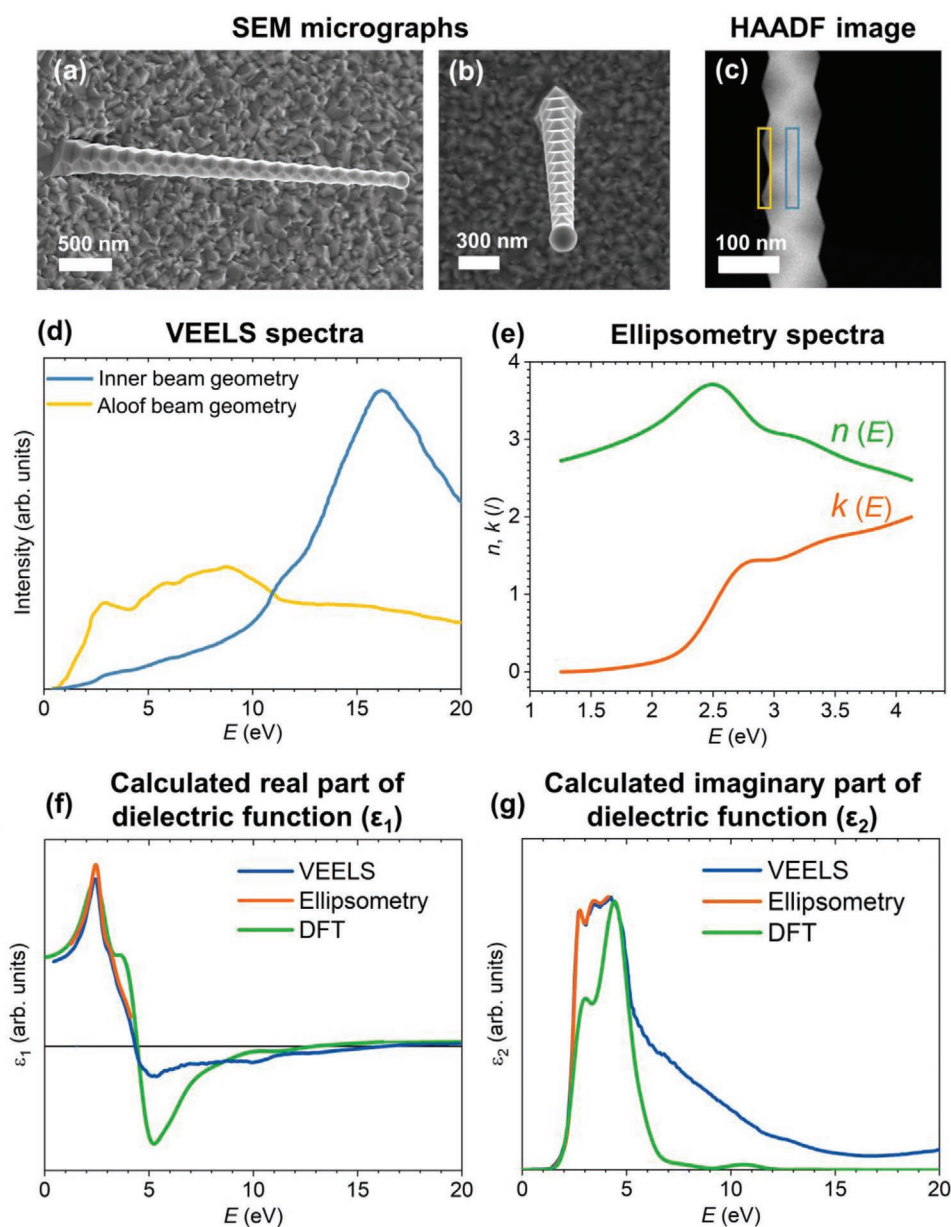


Figure 2. a,b) InLens SEM micrographs of a zigzag Zn_3P_2 nanowire in two different orientations. c) HAADF image of a zigzag Zn_3P_2 nanowire with labeled regions where the VEEL spectra were collected. d) VEEL spectra measured in inner (blue) and aloof beam geometry (orange). e) Refractive index (n) and extinction (k) coefficients of Zn_3P_2 obtained from ellipsometry measurements. Comparison of f) real (ϵ_1) and g) imaginary (ϵ_2) part of the dielectric function obtained from VEELS (blue), ellipsometry measurements (orange), and DFT calculations (green). The intensity of all dielectric functions was normalized to the maximum value, to allow for easier comparison.

values agree well with previously reported ellipsometry studies on polycrystalline samples.^[32,57]

Figure 2f,g compares the real (ϵ_1) and imaginary (ϵ_2) part of the dielectric function obtained from VEELS, ellipsometry measurements, and our own density functional theory (DFT) calculations—more details about the latter are provided in a section further down. The intensity of all dielectric functions was normalized to the maximum value, to allow for easier comparison. The real part ϵ_1 exhibits one oscillation with a maximum at 2.5 eV, followed by the subsequent decrease and a minimum at 5 eV with a further evolution toward zero for energies around

15 eV. The imaginary part ϵ_2 exhibits a broad band, signaling a high absorption coefficient, starting from 2.5 to 6 eV. The experimental ellipsometry and VEELS curves are in excellent agreement within entire range under study. The shape of the curves also agrees very well with the dielectric functions reported in the literature for Zn_3P_2 .^[57] On the other hand, there is some discrepancy between the experimental and theoretically predicted shapes of the dielectric functions. In particular, the main difference between the experiment and theory is in the intensity of the imaginary part. DFT predicts a slightly lower ϵ_2 in the range between 2.8 and 4.8 eV and a faster decay after the maximum at

5 eV. One might attribute the difference in ε_2 intensity to limitations of the local density approximation (LDA) used in the DFT calculations which does not include many body interactions, even though this is rather sensitive to the electronic ground state calculated vibrational properties of this compound, which are found to be in reasonable agreement with experiment.^[58]

2.2. Bandgap Energy and Subbandgap Transitions in Zinc Phosphide

Several methods have been proposed for the determination of the bandgap directly from VEELS, among which the parabolic fit^[59] and derivation method^[60] are the most used ones. Application of these direct methods can be inaccurate, especially when there is not a clear onset in the VEEL spectra. A more reliable way consists of deriving the dielectric functions from VEELS, and calculating the associated absorption coefficient and then extracting the bandgap from the energy dependence.

The dielectric functions can then be related to the absorption coefficient through the following relation:^[22]

$$\alpha(E) = \frac{E}{\hbar c} \left(2(\varepsilon_1^2 + \varepsilon_2^2)^{1/2} - 2\varepsilon_1 \right)^{1/2} \quad (6)$$

where $\hbar = h/2\pi$, with h being the Planck constant, E the energy, and c the speed of light. Based on Tauc's relationship^[61] between the absorption coefficient, α , and the incident energy, E , in the high absorption region of semiconductor:

$$\alpha E = \alpha_0 (E - E_g)^n \quad (7)$$

it is possible to determine the bandgap energy (E_g) and the nature of the transition (n) between the valence and the conduction bands (α_0 denotes a material dependent constant). The nature of transition (n) can vary among the four values: 1/2, 2, 3/2, and 3 that correspond to direct allowed, indirect allowed, direct forbidden, and indirect forbidden transitions, respectively. Assuming that Zn_3P_2 is a direct bandgap semiconductor, the bandgap energy can be determined from the dependence of $(\alpha E)^2$ from E , as shown in Figure S3a, Supporting Information. Linear extrapolation of the curves has yielded Zn_3P_2 bandgap values of 1.50 ± 0.10 and 1.54 ± 0.02 eV for VEELS and ellipsometry measurements, respectively. This is in agreement with previously reported results in the literature.^[32,35] To further justify this, we have extracted the power factor n from the slope of $\ln(\alpha E)$ vs $\ln(E - E_g)$ curve in the high absorption region from 1.5 to 3 eV. We obtain a value of 0.52 ± 0.10 (Figure S3b, Supporting Information). This is very close to 0.5, thus confirming the nature of the 1.5 eV absorption edge to a direct allowed transition.

We would like to point out the remaining low intensity VEELS signal below 1.5 eV (Figure S4, Supporting Information). In general, absorption below the bandgap can be related to a further indirect bandgap or to defect band/level subbandgap transitions. That has been observed in II-Vs; optical emission studies on this material have shown light emission below the bandgap, around 1.3 eV, in both photo and cathodoluminescence.^[32,38,41,56] This is more consistent with the existence of defect bands below the bandgap rather than to an indirect transition. Additional

transitions between the conduction and valence band tails could also contribute to the signal in this region.^[62] Contributions to the VEEL signal below the bandgap energy, occurring due to structural defects or impurities present in the bulk or on the surface of the material, have also been reported for GaN and InN.^[63,64]

2.3. Surface and Volume Plasmons in Zinc Phosphide

We now turn to exploiting the combination of aloof and inner beam geometries to extract information on the surface and bulk plasmons. The dominant and broad peak at $E_p^{\text{exp}} = 16.3 \pm 0.2$ eV in the inner beam response shown in Figure 2d can be attributed to the volume plasmon, which is due to collective excitations of valence electrons triggered by their response to the repulsive field carried by the incident electron. In the case of semiconductors, the free electron model predicts that the volume plasmon energy can be modified by introducing a bound oscillation with frequency $\omega_g = E_g/\hbar$, where E_g is the bandgap energy. Thus, the semi-free electron plasmon energy can be obtained from:^[22]

$$E_p^{\text{theo}} = \sqrt{\frac{\hbar^2 e^2 z \rho}{m_e \varepsilon_0 M} + E_g^2} \quad (8)$$

where e and m_e are electron charge and mass, respectively, ε_0 is the dielectric permittivity of vacuum, $z = 16$ is the number of valence electrons per Zn_3P_2 molecule, $\rho = 4.55 \text{ g cm}^{-3}$ is the density of Zn_3P_2 , and $M = 258.12 \text{ g mol}^{-1}$ is the molecular mass. Using the calculated bandgap of 1.50 ± 0.10 eV, the theoretical model predicts the plasmon at $E_p^{\text{theo}} = 15.4 \pm 0.2$ eV. The experimentally observed plasmon peak is shifted to slightly higher energies, which is due to the interband transitions occurring at lower energies than the plasmon peak, as observed in the imaginary part of the dielectric function in Figure 2g. In this case, the polarization of the bound electrons increases the restoring force on the displaced free electrons, increasing the resonance energy above the free-electron value.^[22]

The volume plasmon peak is not clearly present in the VEEL spectra measured in aloof beam geometry (Figure 2d). This indicates at most a minor contribution of the volume plasmon field. In the geometry considered here and, given the wide direct gap nature of the material, the aloof beam VEEL spectrum is expected to be dominated by a so-called surface plasmon. The surface plasmon corresponds to collective oscillations of free electrons at a surface or interface, and its energy is dependent on the geometry of the interface boundary. This boundary is usually approximated as planar^[65] or spherical,^[66] based on which the relation with the volume plasmon energy can be established. The energy of the surface plasmon can also be affected by the presence of contamination (such as oxides), on the surface of the material.^[66] The zig-zag surface geometry of the Zn_3P_2 nanowire could be approximated with a spherical boundary,^[66] and the surface plasmon energy can then be calculated from the volume plasmon E_p^{theo} as:

$$E_s^{\text{theo}} = \frac{E_p^{\text{theo}}}{\sqrt{3}} \quad (9)$$

The calculated value of $E_s^{\text{theo}} = 8.8$ eV corresponds well with the experimentally observed most intense peak at

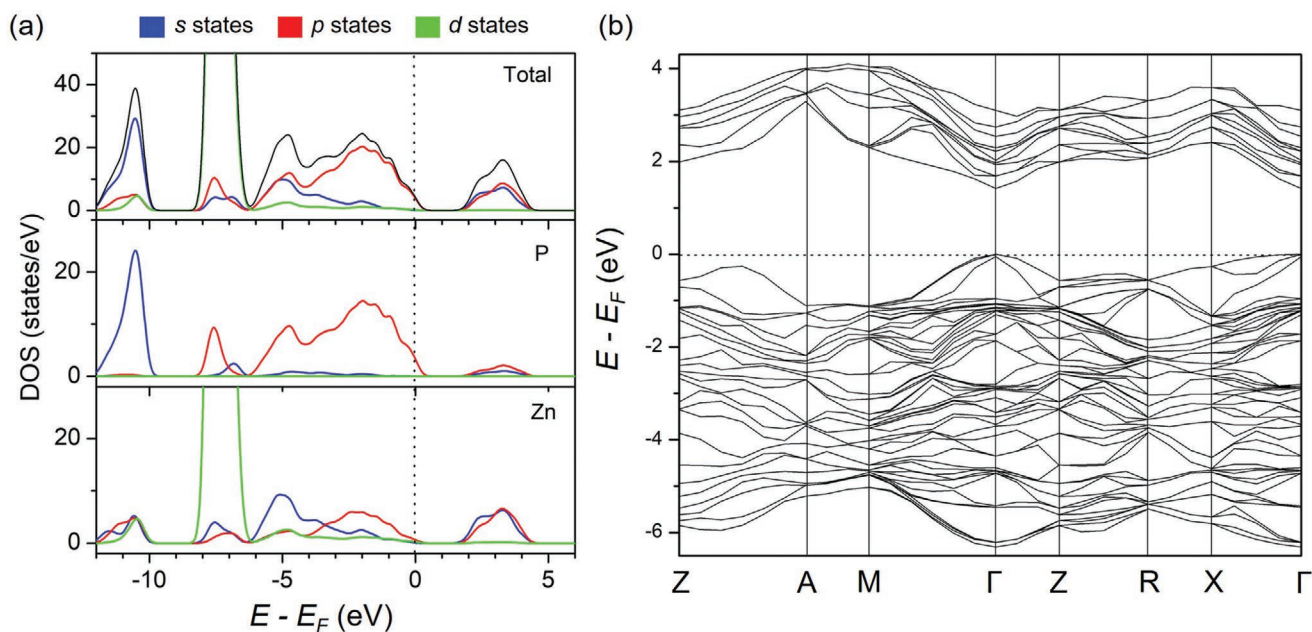


Figure 3. a) Partial and total density of states, and b) electronic band structure of Zn_3P_2 obtained from DFT calculations.

$E_s^{\text{exp}} = 8.7 \pm 0.2 \text{ eV}$ in VEEL spectra measured in a loof beam geometry (Figure 2). This peak can therefore be attributed to surface plasmon excitation.

2.4. Interband Transitions of Zinc Phosphide

We now close the loop by comparing the experimental results with first-principles calculations of the band structure. **Figure 3** presents the total and partial density of states (DOS), as well as the band structure of Zn_3P_2 obtained from DFT calculations (see the Experimental Section for further information about the theoretical calculations).

As evidenced by the partial DOS (PDOS) in Figure 3a, the conduction band is mostly dominated by Zn-*p* and Zn-*s* states, while the P-*p* states dominate the top of the valence band. Contributions of Zn-*d* states and P-*s* states are observed deeper in the valence band.

Based on the band structure shown in Figure 3b, the top of the valence band (within 1 eV from the valence band maximum) is characterized by very dispersive energy bands, in contrast to the lower valence bands where less dispersion is evident. The conduction band onset is characterized by strongly dispersive bands whose energy minima occur at the Γ and Z points, at 1.5 and 2 eV, respectively. This confirms that Zn_3P_2 is a direct bandgap semiconductor, in agreement with the VEELS and ellipsometry measurements.

Using the calculated band structure and (P)DOS, one can correlate and identify the interband transitions observed in the VEEL spectra, as shown in **Figure 4a** and listed in **Table 1**. It is observed that the low energy region, up to the surface plasmon, is dominated by the transitions from P-*p* states in the valence band to Zn-*s* and Zn-*p* states in the conduction band. On the other hand, the higher energy region in the VEEL spectra

corresponds to deep level transitions in the valence band, that is, from Zn-*d* and P-*s* states to Zn-*s* states in the conduction band. From the assignments of the different transition energies to distinct transition processes, a schematic energy level diagram is constructed and plotted in Figure 4b.

It should be noted that geometry dependent modes, such as polaritons or interference modes have been observed in the VEEL spectra of metallic nanowires with different shapes, as reviewed in ref. [26]. Positions of features attributed to such modes in VEEL spectra are often calculated using numerical simulations.^[67,68] Considering that Zn_3P_2 is a semiconductor, therefore a poor plasmonic material, and that all features in the measured VEEL spectra have been attributed to either plasmon excitation or interband transitions, as described above, any contributions from such effects do not appear to play a dominant role in the VEEL spectra of the probed Zn_3P_2 nanowire.

3. Conclusions

Electronic structure investigations of Zn_3P_2 were performed by VEELS and spectroscopic ellipsometry. The experimentally determined transition energies were assigned to distinct interband transitions by comparison to calculated band structures and densities of states, which were obtained by DFT-based calculations. The combination of two different experimental techniques with the first-principles calculations allowed the construction of a schematic energy band diagram for Zn_3P_2 . It was determined that Zn-*p* and Zn-*s* states are dominating in the conduction band, while the P-*p* states are prevailing in the top of the valence band. Deeper levels in the valence bands are attributed to contributions from of Zn-*d* states and P-*s* states. Both theory and experiments have shown that Zn_3P_2 is a direct

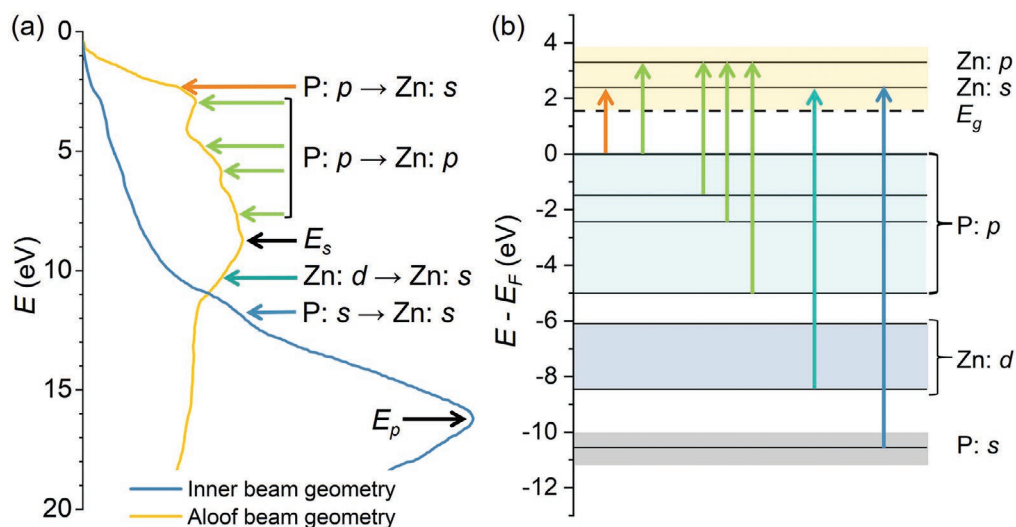


Figure 4. a) Identification of interband transitions in VEELS spectra based on the band structure and P(DOS) obtained from DFT. The arrows indicate the interband transitions, while E_s and E_p denote the energies of the surface and the volume plasmons. b) Schematic energy level diagram for Zn_3P_2 . The transitions from the valence band into the conduction band assigned in this work are plotted according to Table 1. Energies are taken from the band structure and DOS calculations and are calibrated with respect to energy zero at the top of the valence band.

bandgap semiconductor, with a bandgap energy of 1.50 ± 0.10 and 1.52 ± 0.02 eV according to the VEELS and ellipsometry measurements, respectively. The volume and surface plasmon of Zn_3P_2 were observed in the VEEL spectra at 16.3 ± 0.2 and 8.7 ± 0.2 eV, respectively. These values were in good agreement with the theoretically expected plasmon positions according to the semi-free electron model. The calculated real and imaginary dielectric functions from VEELS and ellipsometry measurements have shown an excellent agreement. A larger discrepancy was observed upon the line shape comparison with the theoretically calculated dielectric functions, which was attributed to the approximations used in the DFT calculations. However, the energy positions of the interband transitions were still in good agreement from both theory and experiments. The present results offer significant insights into the electronic band structure of Zn_3P_2 which is crucial for further development of the material and its application in optoelectronic and photovoltaic devices.

Table 1. Identification of interband transitions in Zn_3P_2 .

Transition energy [eV]	Identification
2.4 ± 0.2	P-p to Zn-s
2.9 ± 0.2	P-p to Zn-p
4.9 ± 0.2	P-p to Zn-p
5.9 ± 0.2	P-p to Zn-p
7.7 ± 0.2	P-p to Zn-p
8.7 ± 0.2	E_s
10.3 ± 0.2	Zn-d to Zn-s
12.2 ± 0.2	P-s to Zn-s
16.3 ± 0.2	E_p

4. Experimental Section

Density-Functional Theory Calculations: The first-principles calculations of the electronic ground state of the tetragonally structured Zn_3P_2 were performed within the LDA using the Ceperly–Adler functional,^[69,70] as implemented in the CASTEP code.^[71] Norm-conserving pseudopotentials were used. The cutoff energy for the plane wave basis was set to 600 eV. A self-consistent-field (SCF) tolerance better than 10^{-7} eV per atom and the phonon SCF threshold of 10^{-12} eV per atom were imposed. Prior to performing calculations, the structure was relaxed so that forces on atoms in the equilibrium position did not exceed $2 \text{ meV } \text{ \AA}^{-1}$ and the residual stress was below 5 MPa. Experimentally determined lattice parameters from ref. [72] were used as a starting point. An integration over the Brillouin zone was performed over a $3 \times 3 \times 2$ Monkhorst–Pack grid in reciprocal space.

Material Preparation: Zn_3P_2 was grown using a Veeco GENxplor molecular beam epitaxy system on InP (100) substrates. The growth of nanowires, as explained in more detail in ref. [38], was initiated through a 5 min zinc predeposition at 250 °C to generate In particles by reacting with the substrate, which acted as catalysts for vapor–liquid–solid growth. The nanowires were subsequently grown for 4 h under a Zn flux of 3.4×10^{-7} Torr as measured by a beam flux monitor, and a phosphorus flux of 4.4×10^{-7} Torr (V/II ratio ≈ 1.45). Monocrystalline thin films used for ellipsometry measurements were grown as detailed in ref. [56].

Valence Electron Energy Loss Spectroscopy: VEELS maps were collected on a STEM-dedicated Nion microscope (US100MC) operating at 60 kV equipped with a C5 Nion probe corrector and ultrahigh vacuum (UHV) Gatan Enfium ERS spectrometer. The microscope was equipped with a cold-field emission gun (energy spread ≈ 0.35 eV), used in combination with a monochromator to improve the energy resolution. While higher resolutions were possible, the authors opted to work at ≈ 30 meV energy resolution to achieve a sufficiently high signal-to-noise ratio to accurately observe the VEELS signal. The beam convergence semi-angle was 31.5 mrad, the EEL spectrometer entrance aperture semi-angle was 44 mrad, and HAADF image detector angle was 100–230 mrad. EEL spectrum image acquisition was done using a pixel size of $5.6 \text{ nm} \times 5.6 \text{ nm}$, exposure time per spectrum of 2 s, as well as an energy dispersion of 10 meV/channel. The spectra were then summed using 2×15 spectrum regions from the sections shown in Figure 2c for surface (orange) and core (blue) contributions, respectively. To subtract

the ZLP, a reference spectrum was acquired in vacuum, ≈ 100 nm away from any neighboring structures under the same conditions and in the same session. The reference spectrum was then scaled to fit the part of the ZLP included in the spectral map and applied as a background for direct subtraction using the standard functionalities of Gatan's Digital Micrograph. The reference peak was used to avoid including the full ZLP in the VEEL spectra, as the dynamic range needed would limit the signal-to-noise required to accurately analyze the comparatively small signals in the low-loss region. Figure S5, Supporting Information, shows the uncorrected VEEL spectrum and the reference ZLP that was used for subtraction. In order to minimize contamination, the specimens were baked prior to insertion at 130 °C in vacuum ($\approx 10^{-6}$ Torr), and the microscope column was maintained at UHV.

Ellipsometry Measurements: Ellipsometry measurements were done on a Semilab SE-2000 spectroscopic ellipsometer in the energy range from 1.25 to 5.52 eV. The samples were monocrystalline Zn_3P_2 thin films of a few hundred nanometer thickness on a (100) InP substrate. The ellipsometry model was created and fitted using Semilab's Spectroscopic Ellipsometry Analyzer software.

Supporting Information

Supporting Information is available from the Wiley Online Library or from the author.

Acknowledgements

The authors gratefully acknowledge support from the Swiss National Science Foundation (SNSF) through project BSCGIO_157705 and by the Max Planck-EPFL Center for Molecular Nanoscience and Technology. M.D. thanks funding from H2020 through SMARTCELL project (project number: 101022257). F.S.H., Q.M.R., and the SuperSTEM Laboratory, the UK National Research Facility for Advanced Electron Microscopy, were supported by the Engineering and Physical Sciences Research Council (EPSRC).

Conflict of Interest

The authors declare no conflict of interest.

Author Contributions

A.F.i.M. and Q.M.R. conceived the research and designed the experiments. S.E.S. prepared the samples, S.E.S. and F.S.H. did the VEELS measurements with inputs from Q.M.R. E.Z.S. performed ellipsometry measurements. A.P.L. did the DFT calculations. M.D. analyzed the data, coordinated the simulations, and connected all results. M.D. and A.F.i.M. wrote the paper with inputs from all the authors.

Data Availability Statement

The data that support the findings of this study are available from the corresponding author upon reasonable request.

Keywords

band structures, density-functional theory, nanowires, semiconductors, valence electron energy-loss spectroscopy

Received: June 6, 2021
Revised: June 30, 2021
Published online: July 15, 2021

- [1] A. Jain, S. P. Ong, G. Hautier, W. Chen, W. D. Richards, S. Dacek, S. Cholia, D. Gunter, D. Skinner, G. Ceder, K. A. Persson, *APL Mater.* **2013**, *1*, 011002.
- [2] K. T. Butler, D. W. Davies, H. Cartwright, O. Isayev, A. Walsh, *Nature* **2018**, *559*, 547.
- [3] O. A. von Lilienfeld, K. Burke, *Nat. Commun.* **2020**, *11*, 4895.
- [4] A. Tkatchenko, *Nat. Commun.* **2020**, *11*, 4125.
- [5] M. Aykol, V. I. Hegde, L. Hung, S. Suram, P. Herring, C. Wolverton, J. S. Hummelshøj, *Nat. Commun.* **2019**, *10*, 2018.
- [6] C. Suh, C. Fare, J. A. Warren, E. O. Pyzer-Knapp, *Annu. Rev. Mater. Res.* **2020**, *50*, 1.
- [7] K. T. Butler, J. M. Frost, J. M. Skelton, K. L. Svane, A. Walsh, *Chem. Soc. Rev.* **2016**, *45*, 6138.
- [8] A. Jain, Y. Shin, K. A. Persson, *Nat. Rev. Mater.* **2016**, *1*, 15004.
- [9] J. Linghu, T. Yang, Y. Luo, M. Yang, J. Zhou, L. Shen, Y. P. Feng, *ACS Appl. Mater. Interfaces* **2018**, *10*, 32142.
- [10] S. Curtarolo, G. L. W. Hart, M. B. Nardelli, N. Mingo, S. Sanvito, O. Levy, *Nat. Mater.* **2013**, *12*, 191.
- [11] S. Luo, T. Li, X. Wang, M. Faizan, L. Zhang, *Wiley Interdiscip. Rev.: Comput. Mol. Sci.* **2021**, *11*, e1489.
- [12] S. A. Shevlin, Z. X. Guo, *Chem. Soc. Rev.* **2009**, *38*, 211.
- [13] A. D. Sendek, E. D. Cubuk, E. R. Antoniuk, G. Cheon, Y. Cui, E. J. Reed, *Chem. Mater.* **2019**, *31*, 342.
- [14] D. P. Tabor, L. M. Roch, S. K. Saikin, C. Kreisbeck, D. Sheberla, J. H. Montoya, S. Dwaraknath, M. Aykol, C. Ortiz, H. Tribukait, C. Amador-Bedolla, C. J. Brabec, B. Maruyama, K. A. Persson, A. Aspuru-Guzik, *Nat. Rev. Mater.* **2018**, *3*, 5.
- [15] L. Zhang, Y. Wang, J. Lv, Y. Ma, *Nat. Rev. Mater.* **2017**, *2*, 17005.
- [16] S. Lu, Q. Zhou, Y. Ouyang, Y. Guo, Q. Li, J. Wang, *Nat. Commun.* **2018**, *9*, 3405.
- [17] E. Garnett, L. Mai, P. Yang, *Chem. Rev.* **2019**, *119*, 8955.
- [18] F. Glas, *Phys. Rev. B* **2006**, *74*, 121302.
- [19] L. Güniat, P. Caroff, A. Fontcuberta i Morral, *Chem. Rev.* **2019**, *119*, 8958.
- [20] K. A. Dick, P. Caroff, J. Bolinsson, M. E. Messing, J. Johansson, K. Deppert, L. R. Wallenberg, L. Samuelson, *Semicond. Sci. Technol.* **2010**, *25*, 024009.
- [21] P. Krogstrup, J. Yamasaki, C. B. Sørensen, E. Johnson, J. B. Wagner, R. Pennington, M. Aagesen, N. Tanaka, J. Nygård, *Nano Lett.* **2009**, *9*, 3689.
- [22] R. F. Egerton, in *Electron Energy-Loss Spectroscopy in the Electron Microscope* (Ed: R. F. Egerton), Springer US, Boston, MA **2011**, pp. 111–229.
- [23] P. Y. Yu, M. Cardona, in *Fundamentals of Semiconductors: Physics and Materials Properties* (Eds: P. Y. Yu, M. Cardona), Springer, Berlin **2010**, pp. 17–106.
- [24] R. R. Zamani, J. Arbiol, *Nanotechnology* **2019**, *30*, 262001.
- [25] F. Hayee, L. Yu, J. L. Zhang, C. J. Ciccarino, M. Nguyen, A. F. Marshall, I. Aharonovich, J. Vučković, P. Narang, T. F. Heinz, J. A. Dionne, *Nat. Mater.* **2020**, *19*, 534.
- [26] F. J. García de Abajo, *Rev. Mod. Phys.* **2010**, *82*, 209.
- [27] R. F. Egerton, in *Electron Energy-Loss Spectroscopy in the Electron Microscope* (Ed: R. F. Egerton), Springer US, Boston, MA **2011**, pp. 231–291.
- [28] R. Erni, N. D. Browning, *Ultramicroscopy* **2005**, *104*, 176.
- [29] M. Y. Swinkels, A. Campo, D. Vakulov, W. Kim, L. Gagliano, S. E. Steinvall, H. Detz, M. De Luca, A. Lugstein, E. Bakkers, A. Fontcuberta i Morral, I. Zardo, *Phys. Rev. Appl.* **2020**, *14*, 024045.
- [30] J. M. Pawlikowski, *Infrared Phys.* **1981**, *21*, 181.
- [31] F. Briones, F. Wang, R. H. Bube, *Appl. Phys. Lett.* **1981**, *39*, 805.
- [32] G. M. Kimball, A. M. Müller, N. S. Lewis, H. A. Atwater, *Appl. Phys. Lett.* **2009**, *95*, 112103.
- [33] N. C. Wyeth, A. Catalano, *J. Appl. Phys.* **1979**, *50*, 1403.
- [34] J. Misiewicz, *J. Phys.: Condens. Matter* **1990**, *2*, 2053.

- [35] S. E. Steinvall, E. Z. Stutz, R. Paul, M. Zamani, N. Y. Dzade, V. Piazza, M. Friedl, V. de Mestral, J.-B. Leran, R. R. Zamani, A. Fontcuberta i Morral, *Nanoscale Adv.* **2021**, *3*, 326.
- [36] M. Bhushan, A. Catalano, *Appl. Phys. Lett.* **1981**, *38*, 39.
- [37] W. Shockley, H. J. Queisser, *J. Appl. Phys.* **1961**, *32*, 510.
- [38] S. E. Steinvall, N. Tappy, M. Ghasemi, R. R. Zamani, T. LaGrange, E. Z. Stutz, J.-B. Leran, M. Zamani, R. Paul, A. Fontcuberta i Morral, *Nanoscale Horiz.* **2020**, *5*, 274.
- [39] R. Paul, N. Humblot, S. E. Steinvall, E. Z. Stutz, S. S. Joglekar, J.-B. Leran, M. Zamani, C. Cayron, R. Logé, A. G. del Aguila, Q. Xiong, A. Fontcuberta i Morral, *Cryst. Growth Des.* **2020**, *20*, 3816.
- [40] E. A. Fagen, *J. Appl. Phys.* **1979**, *50*, 6505.
- [41] N. Mirowska, J. Misiewicz, *Semicond. Sci. Technol.* **1992**, *7*, 1332.
- [42] V. Munoz, D. Decroix, A. Chevy, J. M. Besson, *J. Appl. Phys.* **1986**, *60*, 3282.
- [43] L. Bryja, K. Jezierski, J. Misiewicz, *Thin Solid Films* **1993**, *229*, 11.
- [44] J. M. Pawlikowski, J. Misiewicz, N. Mirowska, *J. Phys. Chem. Solids* **1979**, *40*, 1027.
- [45] S. Demers, A. van de Walle, *Phys. Rev. B* **2012**, *85*, 195208.
- [46] N. Y. Dzade, *Phys. Chem. Chem. Phys.* **2020**, *22*, 1444.
- [47] N. Y. Dzade, *ACS Omega* **2020**, *5*, 1025.
- [48] R. Erni, *Ultramicroscopy* **2016**, *160*, 80.
- [49] M. Stöger-Pollach, P. Schattschneider, *Ultramicroscopy* **2007**, *107*, 1178.
- [50] L. Gu, V. Srot, W. Sigle, C. Koch, P. van Aken, F. Scholz, S. B. Thapa, C. Kirchner, M. Jetter, M. Rühle, *Phys. Rev. B* **2007**, *75*, 195214.
- [51] G. L. Tan, L. K. DeNoyer, R. H. French, M. J. Guittet, M. Gautier-Soyer, *J. Electron Spectrosc. Relat. Phenom.* **2005**, *142*, 97.
- [52] F. Paumier, V. Fouquet, M.-J. Guittet, M. Gautier-Soyer, R. H. French, G. Tan, Y. M. Chiang, M. Tang, A. Ramos, S.-Y. Chung, *Mater. Sci. Eng., A* **2006**, *422*, 29.
- [53] B. A. Glassy, B. M. Cossairt, *Chem. Commun.* **2015**, *51*, 5283.
- [54] I. J. Paredes, C. Beck, S. Lee, S. Chen, M. Khwaja, M. R. Scimeca, S. Li, S. Hwang, Z. Lian, K. M. McPeak, S.-F. Shi, A. Sahu, *Nanoscale* **2020**, *12*, 20952.
- [55] A. Henglein, *Chem. Rev.* **1989**, *89*, 1861.
- [56] M. Zamani, E. Z. Stutz, S. E. Steinvall, R. R. Zamani, R. Paul, J.-B. Leran, M. Dimitrievska, A. Fontcuberta i Morral, *J. Phys.: Energy* **2021**, *3*, 034011.
- [57] J. Misiewicz, K. Jezierski, *Solid State Commun.* **1989**, *70*, 465.
- [58] E. Z. Stutz, S. E. Steinvall, A. P. Litvinchuk, J.-B. Leran, M. Zamani, R. Paul, A. Fontcuberta i Morral, M. Dimitrievska, *Nanotechnology* **2020**, *32*, 085704.
- [59] B. Rafferty, L. M. Brown, *Phys. Rev. B* **1998**, *58*, 10326.
- [60] N. D. Browning, I. Arslan, R. Erni, B. W. Reed, in *Scanning Transmission Electron Microscopy: Imaging and Analysis* (Eds: S. J. Pennycook, P. D. Nellist), Springer, New York **2011**, pp. 659–688.
- [61] J. Tauc, *Mater. Res. Bull.* **1968**, *3*, 37.
- [62] P. D. C. King, T. D. Veal, F. Fuchs, Ch. Y. Wang, D. J. Payne, A. Bourlange, H. Zhang, G. R. Bell, V. Cimalla, O. Ambacher, R. G. Egdell, F. Bechstedt, C. F. McConville, *Phys. Rev. B* **2009**, *79*, 205211.
- [63] S. Lazar, G. A. Botton, M.-Y. Wu, F. D. Tichelaar, H. W. Zandbergen, *Ultramicroscopy* **2003**, *96*, 535.
- [64] P. Specht, J. C. Ho, X. Xu, R. Armitage, E. R. Weber, R. Erni, C. Kisielowski, *Solid State Commun.* **2005**, *135*, 340.
- [65] J. M. Pitarke, V. M. Silkin, E. V. Chulkov, P. M. Echenique, *Rep. Prog. Phys.* **2006**, *70*, 1.
- [66] D. Ugarte, C. Colliex, P. Trebbia, *Phys. Rev. B* **1992**, *45*, 4332.
- [67] Y. Cao, A. Manjavacas, N. Large, P. Nordlander, *ACS Photonics* **2015**, *2*, 369.
- [68] U. Hohenester, *Comput. Phys. Commun.* **2014**, *185*, 1177.
- [69] D. M. Ceperley, B. J. Alder, *Phys. Rev. Lett.* **1980**, *45*, 566.
- [70] J. P. Perdew, A. Zunger, *Phys. Rev. B* **1981**, *23*, 5048.
- [71] S. J. Clark, M. D. Segall, C. J. Pickard, P. J. Hasnip, M. I. J. Probert, K. Refson, M. C. Payne, *Z. Kristallogr.* **2005**, *220*, 567.
- [72] I. E. Zanin, K. B. Aleinikova, M. M. Afanasiev, M. Y. Antipin, *J. Struct. Chem.* **2004**, *45*, 844.